IEEE Journal of Translational Engineering in Health and Medicine

Automatic Lung Segmentation With Juxta-Pleural Nodule Identification Using Active Contour Model and Bayesian Approach

**HEEWON CHUNG[1], HOON KO[1], SE JEONG JEON[2], KWON-HA YOON[2],
AND JINSEOK LEE [1], (Senior Member, IEEE)**

[1]Department of Biomedical Engineering, Wonkwang University College of Medicine, Iksan 54538, South Korea
[2]Department of Radiology, Wonkwang University College of Medicine, Iksan 54538, South Korea

CORRESPONDING AUTHOR: J. LEE (gonasago@wku.ac.kr)

ABSTRACT Objective: chest computed tomography (CT) images and their quantitative analyses have become increasingly important for a variety of purposes, including lung parenchyma density analysis, airway analysis, diaphragm mechanics analysis, and nodule detection for cancer screening. Lung segmentation is an important prerequisite step for automatic image analysis. We propose a novel lung segmentation method to minimize the juxta-pleural nodule issue, a notorious challenge in the applications. Method: we initially used the Chan–Vese (CV) model for active lung contours and adopted a Bayesian approach based on the CV model results, which predicts the lung image based on the segmented lung contour in the previous frame image or neighboring upper frame image. Among the resultant juxta-pleural nodule candidates, false positives were eliminated through concave points detection and circle/ellipse Hough transform. Finally, the lung contour was modified by adding the final nodule candidates to the area of the CV model results. Results: to evaluate the proposed method, we collected chest CT digital imaging and communications in medicine images of 84 anonymous subjects, including 42 subjects with juxta-pleural nodules. There were 16 873 images in total. Among the images, 314 included juxta-pleural nodules. Our method exhibited a disc similarity coefficient of 0.9809, modified hausdorff distance of 0.4806, sensitivity of 0.9785, specificity of 0.9981, accuracy of 0.9964, and juxta-pleural nodule detection rate of 96%. It outperformed existing methods, such as the CV model used alone, the normalized CV model, and the snake algorithm. Clinical impact: the high accuracy with the juxta-pleural nodule detection in the lung segmentation can be beneficial for any computer aided diagnosis system that uses lung segmentation as an initial step.

INDEX TERMS Active contour, lung segmentation, chest CT images, computer aided diagnosis, juxta-pleural nodule.

I. INTRODUCTION

Pulmonary or chest computed tomography (CT) images have been used for a variety of purposes, such as lung parenchyma density analysis [1], [2], airway analysis [3], [4], diaphragm mechanics analysis [5], [6] and nodule detection for cancer screening [7]. Recently, with the aid of computing technology, it has become feasible to conduct automatic quantitative analyses. In addition, collaboration among engineers, clinicians, and data scientists has led to the development of accurate automated screening programs for clinical use. Lung segmentation, a step required prior to chest CT imaging analysis, is a crucial starting point for all lung-related quantitative analysis. For instance, in pulmonary nodule detection, when lung segmentation fails to correctly define the borders of the lungs, the nodules outside the borders are missed. One study [8] reported that a computer-aided detection system missed 17% of all true nodules due to erroneous lung segmentations. Thus, an algorithm for automatic and accurate lung segmentation is required.

A large amount of research has been carried out on the topic of lung segmentation in chest CT scans. One of the most common conventional techniques for segmenting lung images

is a thresholding approach [9]–[12], wherein the natural contrast between the low-density lungs and the surrounding high-density chest wall is used for lung segmentation. This approach segments the lung image by identifying large differences in attenuation between the lung parenchyma and the surrounding tissue. Another conventional approach is region growing-based lung image segmentation, which is a type of pixel-based segmentation involving the selection of initial seed points. This approach examines the neighboring pixels of initial seed points and determines whether these pixels are within the target region [8], [13], [14]. In addition, more advanced imaging processing techniques have been proposed, including the deformable model [15]–[17], pattern classification [18], [19], rolling ball [8], graph cut-based methods [20]–[23] and Atlas-based methods [14], [24]–[26], all of which generated robust and accurate results. However, most methods are still limited in their ability to accurately differentiate the surrounding tissue from juxta-pleural nodules, which are attached to the walls of the lung. In some cases, the nodules have the same intensity values as the surrounding tissue [27]. Thus, juxta-pleural nodule detection is one of the most challenging issues in lung segmentation.

Recently, much effort has been directed at detecting the juxta-pleural detection [28]–[30]. In [28], the juxta-pleural nodule was detected by skin boundary detection followed by rough segmentation of lung contour and pulmonary parenchyma refinement. In [29], the initial lung volume segmentation was performed by CV model. Then, non-nodules candidates such as small blood vessels were filtered out using a multiscale Laplacian-of-Gaussian filtering. In [30], intuitionistic fuzzy energy was incorporated into length regularization term of region-based level set method, which resolved the boundary leakage. The all methods provided accurate detection results with the slice by slice processing. However, the performance was limited in the case of the blurred juxta-pleural nodules, which is an inherent limitation. In our work, based on the spatially sliced images from top to bottom, we exploited a Bayesian approach, which predicts and updates lung contour from previously estimated contour.

We first initially used the Chan–Vese (CV) model for active contours. The CV model is a powerful and flexible method that is able to segment many types of images. This model is based on the Mumford–Shah function [31] for segmentation, which has been used widely in the medical imaging field, especially for the segmentation of the brain, heart, and trachea [32]–[35]. While many segmentation methods rely heavily in some way on edge detection, the CV model ignores edges completely. Instead, the method optimally fits a two-phase piecewise constant model to the given image by implicitly representing segmentation boundary with a level set function. It allows the segmentation to handle topological changes more easily than snake methods or other edge detection methods. It also uses the global image information without depending on gradient, which results in better management of image segmentation problems such as strong noise and edge blurs. In addition, it can be applied to images whose gradients are either significant or insignificant; thus, it is suitable for images whose boundaries are either smooth or discontinuous [36]. The CV model was previously evaluated for lung segmentation and found to outperform conventional methods [32], [33], [37].

Nevertheless, the juxta-pleural nodule issue has yet to be resolved [34]. To address this issue, we adopted a Bayesian approach based on the CV model results, which predicts the lung image based on the segmented lung contours in the previous frame image or neighboring upper frame image. Note that the frames represent sequential chest CT images "slices" from top to bottom. This approach is based on the assumption that the lung contour is slightly and uniformly expanded or contracted over frames, while the juxta-pleural nodules have a consistent appearance regardless of the pattern of lung contour changes. Based on our Bayesian approach, we predicted and updated the lung contour over multiple frames. Then, we extracted the difference image by comparing the results from the Bayesian approach and the CV model. Here, each separated group in the difference image corresponds to a juxta-pleural nodule candidate. Finally, we investigated whether the separated groups in the difference image comprised juxta-pleural nodules or portions of the lung wall using concave point detection and circle/ellipse Hough transform. We evaluated the performance of our proposed method by comparing it with the CV model [29], the normalized and modified CV (NM-CV) method [38], [39], and the snake model [40].

The main contributions of this study are:
- We proposed a Bayesian approach for automatic juxta-pleural nodule identification in the lung segmentation stage from chest CT scans.
- We presented a concave point detection and circle/ellipse Hough transform to minimize false positives.
- We tested our proposed method from 16,873 images (84 subjects). Among the images, 314 images included juxta-plerual nodules.
- We further validated the method from different databases, which included 1,766 images in total. Among the images, 125 included juxta-pleural nodules.
- We presented the extension capability that accurate lung contour segmentation results can be provided from any global contour results by applying to our proposed method framework.

II. METHODS
A. COLLECTION OF CHEST CT IMAGES
In the present study, we evaluated our proposed method using chest CT scans from Wonkwang University Hospital (WKUH). For the clinical data, we collected chest CT digital imaging and communications in medicine (DICOM) images of 84 anonymous subjects, including 42 subjects with juxta-pleural nodules. Each scan included 150 to 215 image frames, and there were 16,873 images in total. Among the images, 314 included juxta-pleural nodules. The images were acquired at WKUH using a multiple

detector computed tomography (MDCT) scanner (Somatom Sensation 16, Siemens, Erlangen, Germany; X-ray tube voltage: 100–120 kV; tube current: 80–328 mA; pixel length: 0.56–0.79 mm). The thickness of each slice was 5.0 mm. The WKUH Institutional Review Board approved the collection and analysis of the imaging data. To evaluate the performance of the model, "gold standard" lung contours were obtained from six trained radiologists. Initially, four trained radiologists drew the contours, and another two trained radiologists confirmed them.

B. GLOBAL LUNG CONTOUR EXTRACTION WITH THE CHAN-VESE MODEL

To segment the lung contour, we first applied the CV model to chest CT images . Let Ω be a bounded open subset of R^2 with the boundary $\partial\Omega$. In the evolving lung contour C, as the boundary of an open subset w of Ω, *inside(C)* and *outside(C)* denote the regions w and $\Omega\backslash\overline{ww}$, respectively. The energy term F^G is based on the CV model defined with the length of the contour C, area of the region inside C, and the averages of u_0 inside C and outside C. Accordingly, the energy term F^G is defined by

$$
\begin{aligned}
F^G(c_1, c_2, C) = {} & \mu \cdot Length\,(C) + \nu \cdot Area\,(inside\,(C)) \\
& + \lambda_1 \int_{inside(C)} |u_0\,(x, y) - c_1|^2\,dxdy \\
& + \lambda_2 \int_{outside(C)} |u_0\,(x, y) - c_2|^2\,dxdy \quad (1)
\end{aligned}
$$

where $\mu \geq 0,\ \nu \geq 0,\ \lambda_1, \lambda_2 > 0$ are fixed parameters. *Length(C)* is the length of the lung contour C, and *Area(inside(C))* is the region inside C. $u_0\,(x, y)$ is the pixel intensity in Ω. c_1 and c_2 are the intensity averages of inside C and *outside C*, respectively. The curve C is then found to minimize the global energy term F^G as

$$
\inf_{c_1, c_2, C} F^G\,(c_1, c_2, C) \quad (2)
$$

To find the solution for C, the level set method is used, which replaces the unknown contour C by the level set function $\Phi(x, y)$, where $\Phi(x, y) > 0$ if the point (x,y) is *inside C*, $\Phi(x, y) = 0$ if the point (x,y) is on C, and $\Phi(x, y) < 0$ if the point (x,y) is *outside C*. Then, F^G can be rewritten in terms of $\Phi(x, y)$ as follows:

$$
\begin{aligned}
F^G = F^G\,(c_1, c_2, \emptyset) = {} & \mu \int_\Omega \delta(\emptyset\,(x, y))\,|\nabla\emptyset\,(x, y)|\,dxdy \\
& + \nu \int_\Omega H(\emptyset\,(x, y))dxdy + \lambda_1 \int_{inside(C)} |u_0\,(x, y) \\
& - c_1|^2 H(\emptyset\,(x, y))dxdy + \lambda_2 \int_{outside(C)} |u_0\,(x, y) \\
& - c_2|^2\,(1 - H(\emptyset\,(x, y)))\,dxdy \quad (3)
\end{aligned}
$$

where the first term corresponds to $\mu \cdot Length\,(C)$ and the second term corresponds to $\nu \cdot Area\,(inside\,(C))$. The third and fourth terms correspond to $\lambda_1 \int_{inside(C)} |u_0\,(x, y) - c_1|^2\,dxdy$ and $\lambda_2 \int_{outside(C)} |u_0\,(x, y) - c_2|^2\,dxdy$, respectively. The Heaviside function $H(z)$ is one if $z \geq 0$ and zero if $z < 0$. Its derivative is the one-dimensional Dirac measure $\delta_0(z)$. The minimization problem is solved by taking the Euler–Lagrange equations and updating the level set function

by the gradient descent method as

$$
\begin{aligned}
\frac{\partial\emptyset}{\partial t} = {} & \delta\,(\emptyset) \left[\mu\nabla \cdot \left(\frac{\nabla\emptyset}{|\nabla\emptyset|} \right) - \nu - \lambda_1\,(u_0 - c_1)^2 \right. \\
& \left. + \lambda_2\,(u_0 - c_2)^2 \right] = 0 \text{ in } (0, \infty)\Omega,
\end{aligned}
$$
$$
\emptyset\,(0, \text{x}, \text{y}) = \emptyset_0\,(\text{x}, \text{y}) \text{ in } \Omega,
$$
$$
\frac{\delta_\varepsilon\,(\emptyset)}{|\nabla\emptyset|} \frac{\partial\emptyset}{\partial\vec{n}} = 0 \text{ on } \partial\Omega \quad (4)
$$

where $\vec{n}$ denotes the exterior normal to the boundary $\partial\Omega$, and $\frac{\partial\emptyset}{\partial\vec{n}}$ denotes the normal derivative of $\emptyset$ at the boundary. Here, c_1 and c_2 are updated at each iteration by

$$
\begin{aligned}
c_1\,(\emptyset) &= \frac{\int_\Omega u_0\,(x, y)\,H(\emptyset\,(x, y))dxdy}{\int_\Omega H(\emptyset\,(x, y))dxdy} \\
c_2\,(\emptyset) &= \frac{\int_\Omega u_0\,(x, y)\,(1 - H(\emptyset\,(x, y)))\,dxdy}{\int_\Omega (1 - H(\emptyset\,(x, y)))\,dxdy} \quad (5)
\end{aligned}
$$

For the numerical approximation of the model, the Heaviside function is slightly regularized as

$$
H_\varepsilon\,(z) = \frac{1}{2} \left(1 + \frac{2}{\pi} \arctan\left(\frac{z}{\varepsilon}\right) \right) \quad (6)
$$

where $\varepsilon \to 0$. Then, δ and H can be replaced by δ_ε and H_ε in (4) and (5). For the initialization, we used the checkerboard function in (7) as the level set function, which was used in [41] and [42]. Subsequently, c_1 and c_2 were updated for the initial curve C.

$$
\varphi\,(X) = \sin\left(\frac{\pi}{5}x\right) \sin\left(\frac{\pi}{5}y\right) \quad (7)
$$

After applying with the CV model on the chest CT image, the nodules or vessels inside the lung parenchyma are also segmented. To separate them from the lung contour, we selected the two longest contours, which correspond to left and right lungs. Fig. 1 shows the CV model-based lung segmentation results from four chest CT images. For the CV model-based lung segmentation, we chose the generally used parameters of $\nu = 0$ and $\lambda_1 = \lambda_2 = 1$ in [31]. The parameter of $\mu = 0.01$ was chosen by providing the highest accuracy. As μ increases, the results tend to be roughly segmented. All of the parameters were applied to the entire images in this paper.

The CV model method provided mostly accurate lung wall segmentation results, as shown in Figs. 1(a) to (c). In particular, in Fig. 1(c), the juxta-pleural nodule is included within the segmented lung contour. On the other hand, in Fig. 1(d), the juxta-pleural nodule is outside the segmented lung contour. This is because the pixel intensities of the juxta-pleural nodule and the adjacent surrounding tissue nearly overlap. The juxta-pleural nodule outside the lung contour ultimately results in missed nodules and incorrect quantitative analyses. In the following subsections, we adopted a Bayesian approach to minimize this juxta-pleural nodule issue.
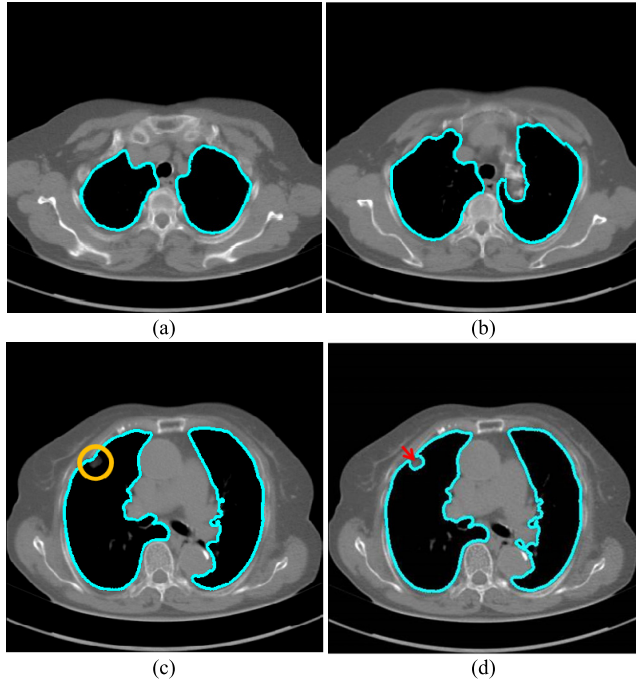
FIGURE 1. Lung segmentation results using Chan–Vese (CV) model. (a) and (b) Most lung contours can be accurately segmented. (c) A correct segmentation results in the presence of a juxta-pleural nodule. (d) An incorrect segmentation results in the presence of a juxta-pleural nodule; The incorrect part is pointed by an arrow.

C. A BAYESIAN APPROACH TO JUXTA-PLEURAL NODULE CANDIDATE DETECTION

Given the N successive chest CT image frames, we denote the lung contour state vector of the n-th image by C_F^n (i.e. $C_F^1, C_F^2, \dots C_F^N$). Note again that the frame represents the spatially sliced image from top to bottom. The state vector C_F^n is assumed to evolve according to the following system model as

$$C_F^n = f_n(C_F^{n-1}, w^n) \qquad (8)$$

where the system transition function f_n corresponds to the change of lung contour at the n-th image from the *(n-1)*-th image. The noise w^n is a zero-mean, white-noise sequence independent of past and current states. In the Bayesian approach, the measurement vector is related to the state vector C_F^n via the observation equation. Here, the measurement vector is C_G^n, which is the result from the CV-based method in (4) and (5). Then, the observation equation can be formulated by

$$C_G^n = h_n(C_F^n, v^n) \qquad (9)$$

where h_n is the measurement function, and the noise v^n is another zero-mean white-noise sequence independent of past and current states and system noise. The initial probability density function (PDF) is $p\left(C_F^1|C_G^0\right) = p(C_F^1)$. The available information at the n-th frame is the set of measurement vectors, such as $D^n = \{C_F^i : i = 1, 2, \dots n\}$.

The requirement is to construct the PDF of the state vector C_F^n, given all the available information of $p(C_F^n|D^n)$, which can be obtained recursively in two stages of prediction and update. Given the required PDF $p(C_F^{n-1}|D^n)$ available, the prior PDF of the state vector C_F^n can be obtained as

$$p\left(C_F^n|D^{n-1}\right) = \int p\left(C_F^n|C_F^{n-1}\right)p\left(C_F^{n-1}|D^{n-1}\right)dC_F^{n-1} \qquad (10)$$

where the first term $p\left(C_F^n|C_F^{n-1}\right)$ is the state evolution based on a Markov model defined by the system transition function f_n and w^n. Then, $p(C_F^n|C_F^{n-1})$ can be formulated by

$$p\left(C_F^n|C_F^{n-1}\right) = \int p\left(C_F^n|C_F^{n-1}, w^n\right)p\left(w^n|C_F^{n-1}\right)dw^n \qquad (11)$$

Since $p\left(w^n|C_F^{n-1}\right) = p(w^n)$,

$$p\left(C_F^n|C_F^{n-1}\right) = \int \delta\left(C_F^n - f_n\left(C_F^{n-1}, w^n\right)\right)p(w^n)dw^n \qquad (12)$$

where $\delta(\cdot)$ is the Dirac delta function. At the n-th frame, a measurement vector C_G^n is available and can be used to update the prior PDF for the posterior PDF via the Bayes rule as

$$p\left(C_F^n|D^n\right) = \frac{p\left(C_G^n|C_F^n\right)p\left(C_F^n|D^{n-1}\right)}{p\left(C_G^n|D^{n-1}\right)} \qquad (13)$$

where the normalizing denominator is

$$p\left(C_G^n|D^{n-1}\right) = \int p\left(C_G^n|C_F^n\right)p\left(C_F^n|D^n\right)dC_F^n \qquad (14)$$

The conditional PDF $p\left(C_G^n|C_F^n\right)$ is defined by the measurement function h_n and v^n as

$$p\left(C_G^n|C_F^n\right) = \int \delta\left(C_G^n - h_n\left(C_F^n, v^n\right)\right)p(v^n)dv^n \qquad (15)$$

In the update stage in (13), the measurement vector C_G^n is used to modify the predicted prior PDF in (10) to obtain the required posterior PDF of the state vector C_F^n. Then, the updated posterior PDF is used for the prior PDF at the *(n+1)*-th frame. The recurrence relations of (10) and (13) constitute the formal solution to the Bayesian recursive estimation problem. More specific prediction and update stages are described in the next subsections.

1) PREDICTION STAGE
Given the contour C_F^{n-1}, we formed the prior $p\left(C_F^n|D^{n-1}\right)$ in (10) by dilating and contracting C_F^{n-1} as shown in Fig. 2(a). The blue areas are dilated curve samples, and the red areas are contracted curve samples. The dilated curves were sampled moving each pixel of C_F^{n-1} toward the normal vector, and the contracted curves were sampled moving each of C_F^{n-1} toward the opposite normal vector. Each pixel movement for dilation and contraction was from 1 to 5 pixels. In [43], solid nodules smaller than 6 mm do not require routine follow-up in patients since there is a paucity of direct evidence regarding caner probability in small nodules. Thus, we limited the
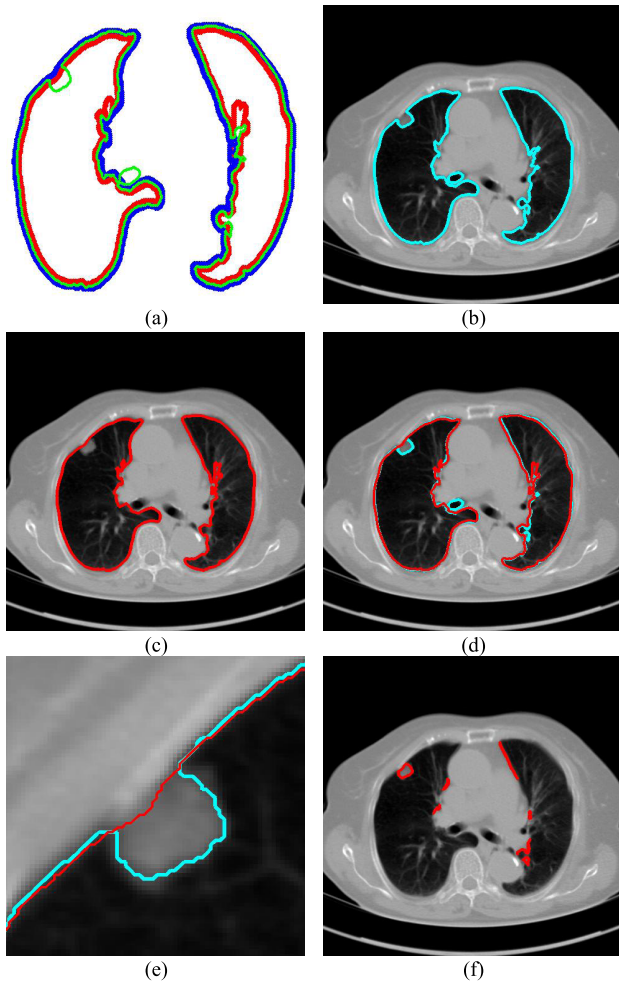
FIGURE 2. (a) Curve samples by $C_F^{*n(i)}$ for dilation (blue) and contraction (red) from C_F^{n-1} (b) global contour C_G^n (c) contour sample C_F^{*n} providing the highest correlation value between C_G^n and each curve from $C_F^{*n(i)}$, (d) the overlapped contours of C_G^n and C_F^{*n}, (e) enlarged and highlighted juxta-pleural nodule area, and (f) the resultant juxta-pleural nodule candidates.

scope to identify the Juxta-pleural nodules smaller than 3mm. Note that the 5 pixel length corresponds to approximately 3mm in the images. Thus, the number of pixels needs to be adjusted according to each different image resolution. The total 10 curve samples represent the prior $p\left(C_F^n|D^{n-1}\right)$ with the system transition function f_n considering dilation and contraction at the *n*-th frame from the (*n-1*)-th frame. Here, we ignore the noise w^n. We denote the predicted curve samples by $C_F^{*n(i)}$.

2) UPDATE STAGE

Given the measurement vector C_G^n obtained from the CV-based method in (4) and (5), we evaluated the likelihood of each contour sample $C_F^{*n(i)}$ to find the best-fitted prediction curve with C_G^n since the lung evolution degree in dilatation or contraction is not exactly known. Hence, we found the best-fitted prediction curve by evaluating the cross-correlation. We first calculated the cross-correlation

between C_G^n and each $C_F^{*n(i)}$, and found that the updated contour sample C_F^{*n} provided the highest correlation values for the left and right lungs. Fig. 2(b) shows the CV model-based contour C_G^n, and Fig. 2(c) shows the resultant updated contour sample C_F^{*n}. Note that the area inside C_G^n does not include the nodule, while the area inside C_F^{*n} does include the nodule. Fig. 2(d) shows the overlapping contours of C_G^n and C_F^{*n}. For better visualization, we enlarged and highlighted the juxta-pleural nodule area as shown in Fig. 2(e). In the next step, we obtained the difference image between the results from the Bayesian approach and the CV model by finding the segments that were simultaneously outside the contour C_G^n and inside the contour C_F^{*n}. The separated segments are the juxta-pleural nodule candidates. Fig. 2(f) shows the resultant nodule candidates. Then, the lung contour can be modified by adding the nodule candidates to the area of C_G^n, which may form the lung contour C_F^n.

D. ELIMINATION OF FALSE POSITIVES

For classifying the nodule candidates as true nodules or false positives, we first investigated whether each candidate contour included any concave point from the center point of C_G^n. Let us denote the set of contour points of each nodule candidate by

$$P_c^{n(i)} = \left\{ P_c^{n(i,j)} : j = 1, 2, \ldots J \; and \; i = 1, 2, \ldots I \right\}, \quad (16)$$

where I is the total number of nodule candidates and J is the total number of contour points for the *i*-th nodule candidate. We calculated the included angle $\angle OP_c^{n(i,j)}Q$, and declared the point $P_c^{n(i,j)}$ to be a concave point if the angle was less than 90°, as illustrated in Fig. 3(a). To calculate the angle $\angle OP_c^{n(i,j)}Q$, we first determined the directions of clockwise and counterclockwise rotation with $P_c^{n(i,j)}$ and found the fifth points next to P_c^n in each direction. Subsequently, we drew the two lines by connecting each of two points to $P_c^{n(i,j)}$. We denote the resultant angles by θ_{in} and θ_{out}, where $0° \leq \theta_{in} < 180°$ and $180° \leq \theta_{out} < 360°$. We additionally drew the line $\overline{P_c^{n(i,j)}Q}$ dividing θ_{out} equally, where point Q is any point in the drawing direction. Fig. 3(b) shows the angle $\angle OP_c^{n(i,j)}Q$ computation examples for the concave point declaration based on the results of Fig. 2(f). In the example, the point $P_c^{n(i,j)}$ from the nodule candidate (top left) is declared to be a concave point, while the point $P_c^{n(i,j)}$ from the false positive (bottom left) is declared to be a non-concave point. Fig. 3(c) shows the detected concave points with red dots on C_G^n. More specifically, Fig. 3(d) shows the detected concave points on the juxta-pleural nodule candidate contours. Finally, only the nodule candidates including concave points remained, as shown in Fig. 3(e).

In the last step, we found the circle/ellipse shape segments among the remaining nodule candidates. For circle/ellipse shape detection, we used a circular Hough transform [44]. We computed the circle/ellipse similarity metric S for each segment, and considered only the segments with $S \geq S_{TH}$, where $S_{TH} = 0.49$, which was optimized using the
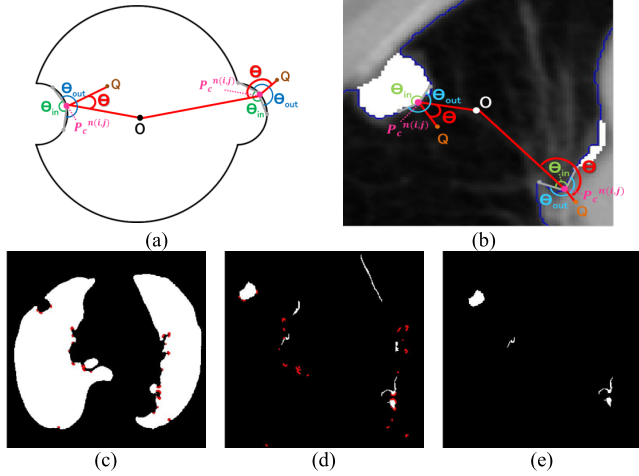
FIGURE 3. (a) Calculation of the included angle $\angle OP_c^{n(i,j)}Q$, and declaration of the point $P_c^{n(i,j)}$ to be a concave point if the angle was less than 90°. (b) Angle $\angle OP_c^{n(i,j)}Q$ computation examples for the concave point declaration based on the results of Fig. 2(f). (c) Detected concave points with red dots on C_G^n. (d) Detected concave points on the juxta-pleural nodule candidate contours, and (e) the remaining nodule candidates that included any concave point.

receiver operating characteristic (ROC) curve as detailed in the Results section. Fig. 4(a) shows the similarity metric S for each remaining segment, and Fig. 4(b) shows the two remaining segments for which where S was greater than 0.49. Subsequently, the area of the remaining segments (yellow contours) were added to the area *inside C_G^n* as shown in Fig. 4(c). Then, the lung contour was finally modified by adding the nodule candidates to the area *inside C_G^n*, which forms the final lung contour, as shown in Fig. 4(d).

E. PERFORMANCE EVALUATION

The performance of our proposed method was evaluated using five metrics: the disc similarity coefficient (DSC), modified Hausdorff distance (MHD), sensitivity, specificity, and accuracy. To compute the five metrics, we first calculated the true positive (TP), false positive (FP), true negative (TN), and false negative (FN) values. TP (FP) is the number of positive pixels labeled correctly (incorrectly). TN (FN) is the number of negative pixels labeled correctly (incorrectly). We used an example to quantize the parameters in Fig. 5. In Fig. 5 (a), the gold standard contour (purple) and the estimated contour (blue) are shown, and the corresponding TP, FP, TN, and FN are shown in Fig. 5(b). Each estimated contour was evaluated with each gold standard contour for all images.

Based on the four parameters, the DSC can be calculated as

$$DSC = \frac{2TP}{2TP + FP + FN} \qquad (17)$$

The DSC is the most commonly used metric for determining the segmentation of false positives and false negatives. It is a statistical approach used to compare the similarity of two data sets, which we used to determine the similarity
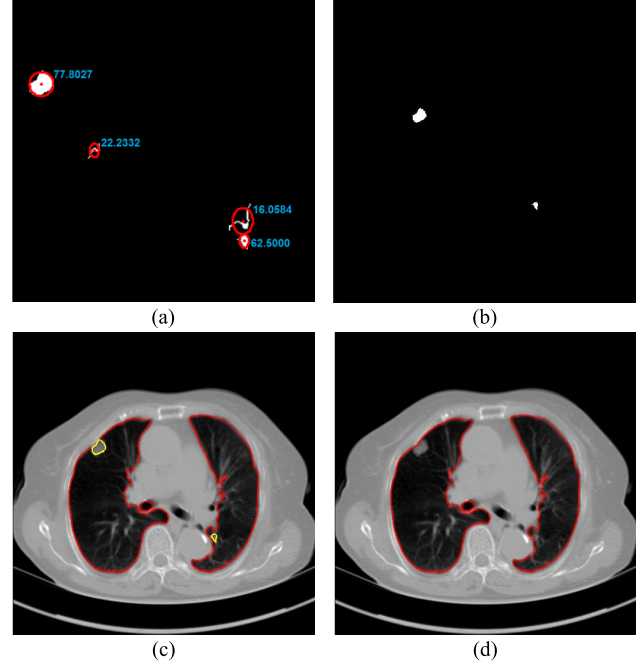

FIGURE 4. (a) Similarity metric *S* for each remaining segment. (b) Two remaining segments where *S* was greater than 0.49. (c) Areas of the remaining segments (yellow contours) were added to the area *inside C_G^n*. (d) Final lung contours were defined by adding the nodule candidates to the area *inside C_G^n*.
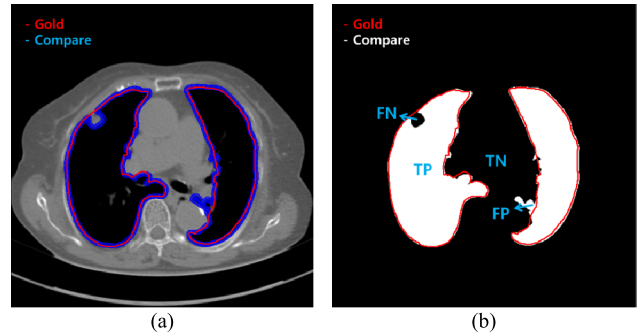

FIGURE 5. (a) Example of the gold standard contour (purple) and estimated contour (blue), and (b) the corresponding true positive (TP), true negative (TN), false positive (FP), and false negative (FN).

between the estimated contour and the gold standard. The DSC value ranges between 0 and 1, where 0 means that there is no similarity and 1 means that there is perfect similarity. The MHD measures how far two subsets of a metric space are from each other. It computes the forward and reverse distances and outputs the minimum of both [37]. The other metrics of sensitivity, specificity, and accuracy were calculated as

$$\text{Sensitivity} = \frac{TP}{TP + FN}$$
$$\text{Specificity} = \frac{TN}{TN + FP}$$
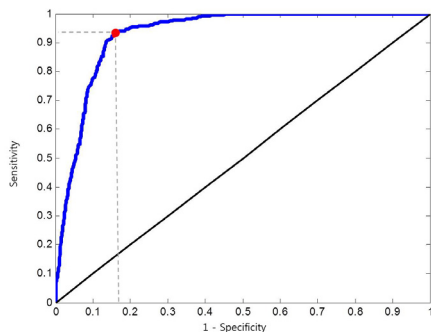$$\text{Accuracy} = \frac{TP + TN}{TP + TN + FP + FN} \qquad (18)$$

FIGURE 6. Receiver operating curve (ROC) curve with 1 minus specificity versus sensitivity in 0.01 increments from 0 to 1.

To evaluate our proposed method, we implemented the CV model [29], the normalized CV (NM-CV) model [38], [39], and the snake algorithm [40], and compared the results with those of our proposed method, based on chest CT images including juxta-pleural nodules ($N = 314$) from 42 subjects, and all chest CT images ($N = 16, 873$) from 84 subjects. For the snake algorithm [45], [46], the parameters of length (α), curvature (β) and smoothing spline (λ) were used with 0.001, 0 and 100, respectively in [46].

To assess significant differences, we performed one-way analysis of variance (ANOVA) tests with Bonferroni corrections for multiple comparisons ($p < 0.05$) using SPSS ver.18 (SPSS Inc., Chicago, IL, USA).

The Matlab codes of our proposed method is available online both at https://sites.google.com/site/bamilab/source-codes/lung-segmentation and https://github.com/Heewon Chung92/LungSegmentation.

III. RESULT

A. ROC EVALUATION ON S_{TH}

We computed the circle/ellipse similarity metric S for the remaining nodule candidates ($N = 1, 079$) after the concave point identification based on the all images. To find the optimum threshold value S_{TH}, we adjusted the metric S from 0 to 1 in 0.01 increments, and evaluated the ROC curve. Fig. 6 shows the ROC curve with 1 minus specificity versus sensitivity for S. For the ROC evaluation, we found the values for TP, TN, FP, and FN, and then calculated the sensitivity, specificity, and accuracy. The best accuracy was found to be 0.9442 with $S_{TH} = 0.49$, which is also the closest to the upper left corner (Fig. 6).

B. PERFORMANCE EVALUATION AND COMPARISON

Fig. 7 shows several examples of lung segmentation results using our proposed method (rightmost panels) compared with the CV model (leftmost panels), NM-CV model (second left panels) and snake algorithm (second right panels). The juxta-pleural nodules resulted in incorrect lung segmentation for the CV model, NM-CV model, and snake algorithm. On the other hand, our proposed method correctly segmented the lung, including juxta-pleural nodules within the lung contour

area. For example, in Fig. 7(a), the juxta-pleural nodule has similar intensity values compared with the surrounding tissue. The CV model, NM-CV model, and snake algorithm generated contours that excluded the nodules. Similar results can be observed in other conventional approaches, such as thresholding and region growing.

In our proposed method, the CV model-based result C_G^n and the predicted contour sample $C_F^{*n(i)}$ from C_F^{n-1} were evaluated for likelihood based on cross-correlation. Subsequently, the contour sample C_F^{*n} update, followed by concave point detection and Hough transform, could detect the juxta-pleural nodule and modify the results by adding the nodule to the area inside C_G^n, which finally segmented the lung contour C_F^n as shown in the rightmost panel of Fig. 7(a). Figs. 7(b) through (h) also show that our proposed method detected juxta-pleural nodules and correctly segmented lung contours. Therefore, using the combination of the CV model and the Bayesian approach, we achieved accurate lung segmentation and successfully detected juxta-pleural nodules.

To further evaluate our proposed method, we compared the results from the CV model, NM-CV model, the snake algorithm and our proposed method on the CT images that included juxta-pleural nodules ($N = 314$). We computed the DSC, MHD, sensitivity, specificity, and accuracy. Fig. 8 shows the distribution of these metrics. The squares at the top and bottom represent the 90th and 10th percentiles, respectively. The whiskers at the top and bottom represent the 75th and 25th percentiles, respectively, and the circle indicates the median value. Regarding the DSC, our proposed method provided the highest DSC mean value (0.9712), while the CV model, NM-CV model, and the snake algorithm provided mean values of 0.8410, 0.8428, and 0.8198, respectively. Our proposed method provided the lowest MHD mean value (0.4504), while the CV model, NM-CV model, and the snake algorithm provided mean values of 2.1727, 2.1486, and 2.2573, respectively. Our proposed method also provided the highest sensitivity value, 0.9711, while the CV model, NM-CV model, and the snake algorithm provided values of 0.0.7366, 0.7389, and 0.7040, respectively. Regarding accuracy, our proposed method also provided the highest value, 0.9667, while the CV model, NM-CV model and the snake algorithm provided values of 0.8050, 0.8072, and 0.7843, respectively. All of the above results were statistically significant. On the other hand, in our proposed method, the mean specificity value was 0.9637, which was slightly lower than that provided by the other methods. However, the difference was not statistically significant. Furthermore, using our proposed method we could detect 96% of the juxta-pleural nodules and correctly modify the lung contour; conversely, the CV method, NM-CV model, and snake algorithm could detect only 11%, 14%, and 9% of the juxta-pleural nodules, respectively. Table 1 summarizes the results of our comparisons.

Finally, we performed our proposed method on all chest CT images ($N = 16, 873$). Table 2 summarizes the performance of all models in terms of the DSC, MHD,
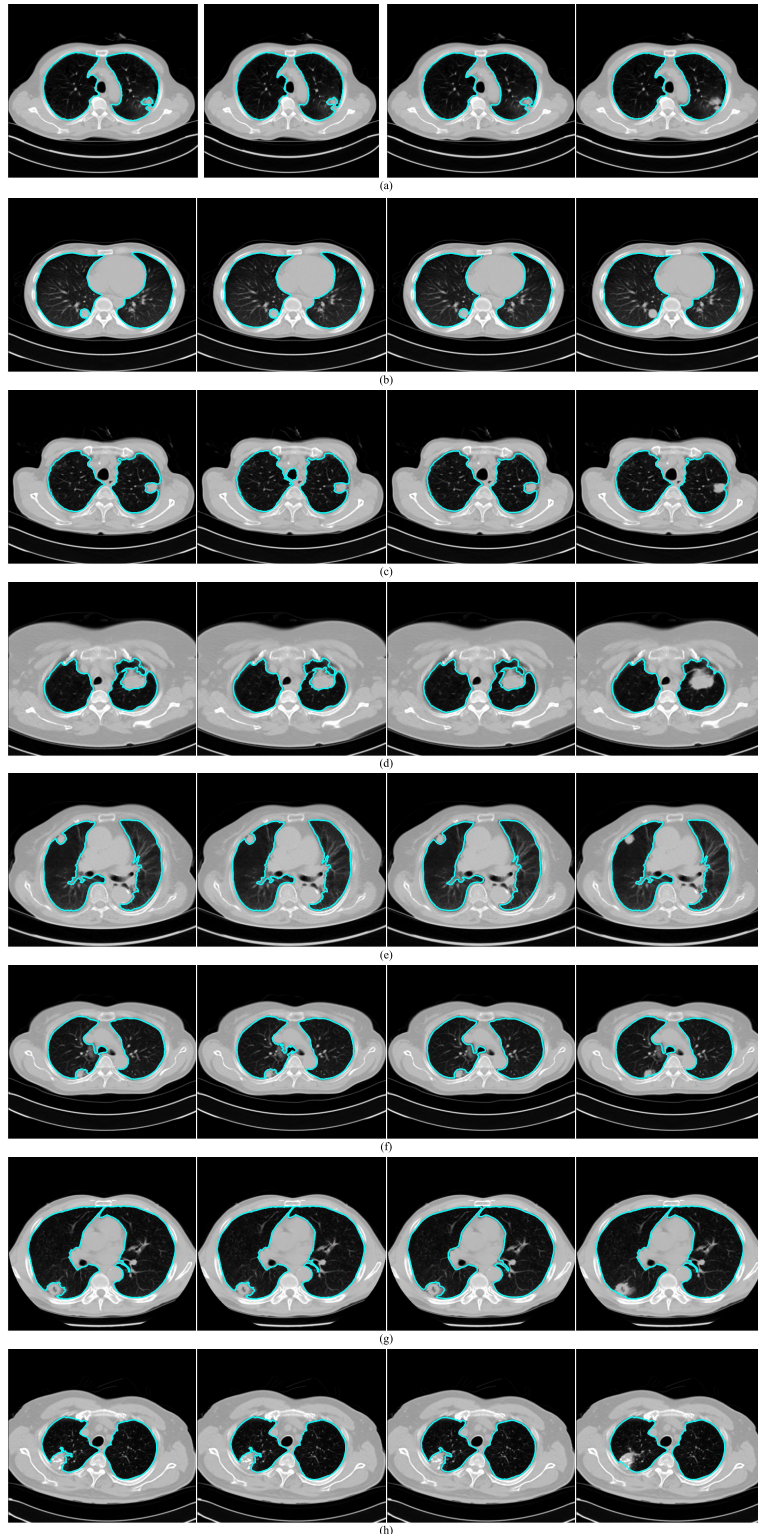
FIGURE 7. Performance comparison for juxta-pleural nodules: (top left) the CV model, (top right) normalized modified Chan–Vese (NM-CV) model, (bottom left) the snake algorithm, and (bottom right) our proposed method. The performance comparison shown from (a) through (h) includes several juxta-pleural nodule cases.

sensitivity, specificity, and accuracy. Our proposed method provided the highest mean DSC value (0.9709), while the CV model, NM-CV model, and snake algorithm provided

mean values of 0.9692, 0.9693, and 0.9684, respectively. Our method provided the lowest mean MHD value (0.5006), compared with 0.5191, 0.5162, and 0.5227 for the CV model,
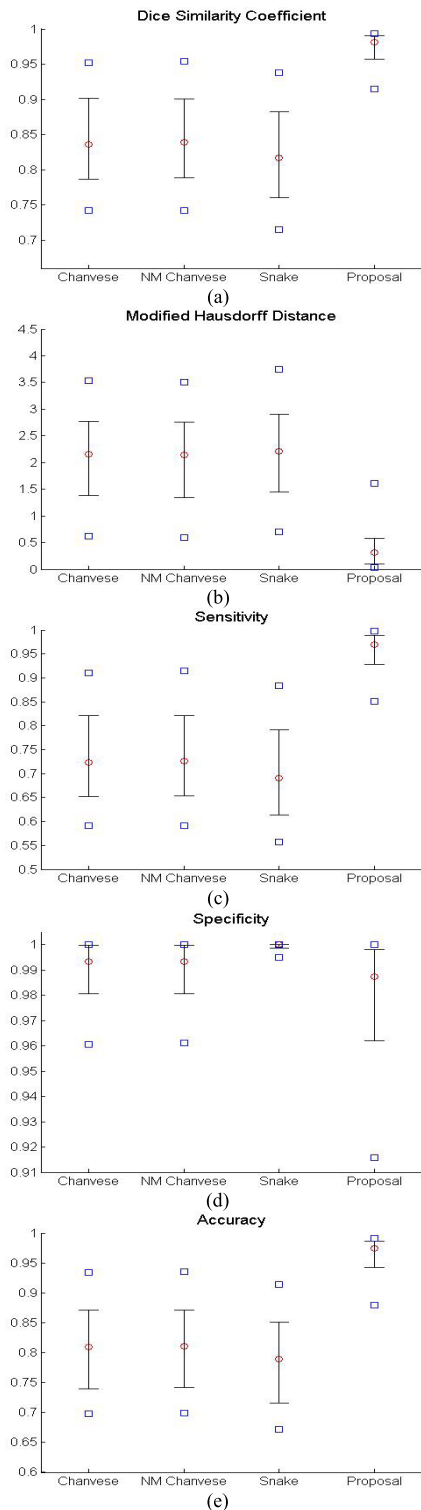
FIGURE 8. Comparison of the four methods: the distribution of the disc similarity coefficient (DSC), modified Hausdorff distance (MHD), sensitivity, specificity, and accuracy. The squares at the top and bottom represent the 90th and 10th percentiles, respectively. The whiskers at the top and bottom represent the 75th and 25th percentiles, respectively, and the circle indicates the median value.

NM-CV model, and snake algorithm, respectively. Our proposed method also provided the highest sensitivity and accuracy values: 0.9585 and 0.9954, respectively. Regarding

TABLE 1. Comparison of the performance of the four methods on CT images that included juxta-pleural nodule ($N = 314$). The DSC, MHD, sensitivity, specificity, accuracy, and juxta-pleural nodule detection rate were evaluated and compared. Mean, standard deviation and detection rate are summarized.

Method		CV	NMCV	Snake	Proposed method
DSC	mean	0.8410	0.8428	0.8198	0.9712
	std	0.0801	0.0782	0.0866	0.0251
MHD	mean	2.1727	2.1486	2.2573	0.4504
	std	1.1679	1.1485	1.1945	0.4433
Sensitivity	mean	0.7366	0.7389	0.7040	0.9711
	std	0.1198	0.1180	0.1243	0.0331
Specificity	mean	0.9854	0.9855	0.9983	0.9637
	std	0.0208	0.0216	0.0042	0.0716
Accuracy	mean	0.8050	0.8072	0.7843	0.9667
	std	0.0972	0.0944	1.005	0.0241
Detection rate (%)		11%	14%	9%	96%

TABLE 2. Results of comparison of the four methods on all chest CT images ($N = 16, 873$). The DSC, MHD, sensitivity, specificity and accuracy were evaluated. The mean and standard deviation are summarized.

Method		CV	NMCV	Snake	Proposed method
DSC	mean	0.9692	0.9693	0.9684	0.9709
	std	0.0524	0.0513	0.0514	0.0511
MHD	mean	0.5191	0.5162	0.5227	0.5006
	std	0.5978	0.5837	0.5927	0.5771
Sensitivity	mean	0.9550	0.9554	0.9543	0.9585
	std	0.0728	0.0722	0.0746	0.0722
Specificity	mean	0.9992	0.9991	0.9993	0.9981
	std	0.0015	0.0013	0.0017	0.0012
Accuracy	mean	0.9952	0.9953	0.9951	0.9954
	std	0.0129	0.0128	0.0132	0.0129

specificity, the mean specificity value (0.9981) was slightly lower than the other methods by the cost of increased sensitivity. Table 2 summarizes the results of the comparison.

C. DISCUSSION ON EFFECT OF PREDICTION ORDER AND LIMITATIONS

Given the contour C_F^{n-1}, we formed the prior $p\left(C_F^n | D^{n-1}\right)$ as previously described (10) by dilating and contracting C_F^{n-1}. In (10), the term $p(C_F^n | C_F^{n-1})$ is the state evolution based on a Markov model defined by the system transition function f_n and w^n. Throughout this paper, we considered the first-order prediction order for the curve samples $C_F^{*n(i)}$. Here, we may consider higher-order predictions. In second-order or higher predictions, the predicted curve samples $C_F^{*n(i)}$ can be obtained from C_F^{n-K}, where K is the prediction order. It is useful to use the curves C_F^{n-K} when C_F^{n-1} is not accurate or when its area inside the contour does not include a juxta-pleural nodule. If the area inside the curve C_F^{n-1} does not correctly include a juxta-pleural nodule, the predicted curve samples $C_F^{*n(i)}$ cannot further include the nodule in the final result C_F^n. Furthermore, the successive incorrect C_F^n can continuously and incorrectly evolve in the following frames (i.e. at the $n+1$, $n+2$, … frame). Hence, to avoid this issue, we may consider higher-order predictions by formulating the

prior PDF of the state vector C_F^n as

$$p\left(C_F^n|D^{n-1}\right)$$
$$= \sum_{k=1}^{K} \int p\left(C_F^n|C_F^{n-k}\right) p\left(C_F^{n-k}|D^{n-k}\right) dC_F^{n-k} \quad (19)$$

This use of higher-order predictions is based on the assumption that the lung contour does not change rapidly in consecutive frames. Fig. 9 shows the distribution of correlation values between consecutive frames of lung images from the clinical database ($N = 16,873$). It shows that the median correlation value between consecutive lung images at the nth frame and the $(n-1)$-th frame is 0.9842 for the right lung and 0.9849 for the left lung. Regarding the lung images between the nth frame and the $(n-2)$-th frame, the correlation median value is slightly lower: 0.9745 for the right lung and 0.9756 for the left lung. However, such second-order or higher predictions may decrease the accuracy of the predicted lung morphology, which may degrade the overall performance in terms of the DSC, MHD, sensitivity, specificity, and accuracy.
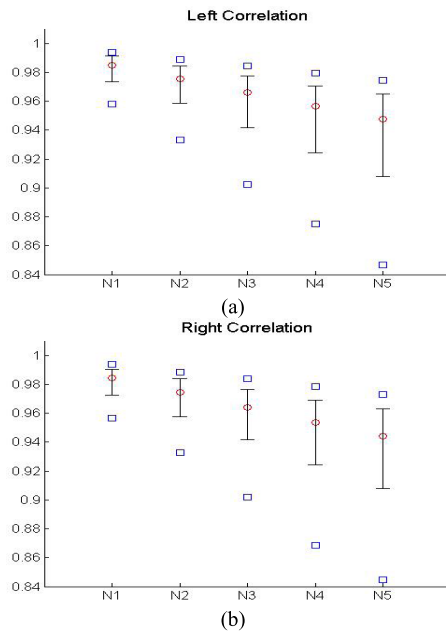

FIGURE 9. Distribution of correlation values between consecutive frame lung images from the clinical database ($N = 16,873$): (a) left lung image correlation and (b) right lung image correlation.

To investigate the effect of the order of predictions, we compared the results of first- and second-order predictions ($K = 1$ and 2). When $K = 2$, the prior PDF of the state vector C_F^n can be formulated as

$$p\left(C_F^n|D^{n-1}\right) = \sum_{k=1}^{2} \int p\left(C_F^n|C_F^{n-k}\right) p\left(C_F^{n-k}|D^{n-k}\right) dC_F^{n-k}$$
$$(20)$$

Then, we formed the prior $p\left(C_F^n|D^{n-1}\right)$ by dilating and contracting both C_F^{n-1} and C_F^{n-2}. The total 20 curve samples

represent the prior $p\left(C_F^n|D^{n-1}\right)$ with the system transition function f_n considering dilation and contraction at the nth frame from both the $(n-1)$-th and the $(n-2)$-th frames. We compared the results from $K = 1$ and 2 on the CT images that included juxta-pleural nodules ($N = 314$), as well as the DSC, MHD, sensitivity, specificity, accuracy, and juxta-pleural nodule detection rate. When $K = 2$, the juxta-pleural nodule detection rate increased from 90% to 98%. However, even with the aid of the contour modification from the detected nodule, the DSC, MHD, sensitivity, specificity, and accuracy were all worse than when $K = 1$. These results were all statistically significant. The results can be explained by the fact that higher-order prediction decreases the overall accuracy of the predicted lung morphology, which eventually degrades the overall performance in terms of the DSC, MHD, sensitivity, specificity, and accuracy. Table 3 summarizes the results of the comparison.

TABLE 3. Results of the comparison of $K = 1$ and 2 on CT images that included juxta-pleural nodules ($N = 314$). The DSC, MHD, sensitivity, specificity, accuracy, and juxta-pleural nodule detection rate were evaluated and compared. Mean, standard deviation and detection rate are summarized.

Method		K = 1	K = 2
DSC	*mean*	0.9712	0.9025
	std	0.0251	0.0887
MHD	*mean*	0.4504	1.5042
	std	0.4433	1.5099
Sensitivity	*mean*	0.9711	0.8850
	std	0.0331	0.1358
Specificity	*mean*	0.9637	0.9396
	std	0.0716	0.0541
Accuracy	*mean*	0.9667	0.8741
	std	0.0241	0.1089
Detection rate (%)		96%	98%

We also compared the results when $K = 1$ or 2 on all chest CT images ($N = 16,873$). Table 4 summarizes the comparative performance in terms of the DSC, MHD, sensitivity, specificity, and accuracy. As expected, all metrics showed that the results when $K = 1$ were superior to those when $K = 2$. These results were also all statistically significant. Thus, in the future, we need to consider an adaptive approach with variable prediction order that maintains both high segmentation accuracy and high juxta-pleural nodule detection rate.

Given the number of juxta-pleural nodule candidates, the elimination of false positives is a critical step. In our method, irregularly shaped nodule candidates were filtered out through the circle/ellipse detection step. However, the detection of irregularly shaped nodules is crucial in not only automatic lung segmentation but also in automatic nodule detection inside the segmented contour: cancerous nodules are more likely to have irregular shapes, rougher surfaces, and color variations or speckled patterns. Fig. 10 shows the juxta-pleural irregular shape nodules in our clinical database. Unfortunately, those were all filtered out during the circle/ellipse detection step. The missing irregular shape

TABLE 4. Results of the comparison of $K = 1$ and 2 on all chest CT images ($N = 16, 873$). The DSC, MHD, sensitivity, specificity, and accuracy were evaluated and compared. Mean and standard deviation are summarized.

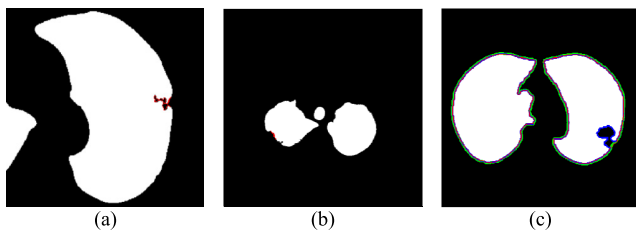| Method		K = 1	K = 2
DSC	*mean*	0.9709	0.7323
	std	0.0511	0.1152
MHD	*mean*	0.5006	1.4270
	std	0.5771	0.5586
Sensitivity	*mean*	0.9585	0.7755
	std	0.0722	0.0697
Specificity	*mean*	0.9981	0.7322
	std	0.0012	0.1329
Accuracy	*mean*	0.9954	0.7321
	std	0.0129	0.1517

FIGURE 10. Irregularly shaped juxta-pleural nodules in our clinical database. (a), (b) and (c): The nodules filtered out completely from the circle/ellipse detection step.

nodule is one of the limitations of our proposed method. Thus, further rigorous research is required for the detection of juxta-pleural nodules without incurring the cost of false positives.

Another limitation is that our proposed method cannot identify the nodule if the nodule is first appeared inside the lung parenchyma and becomes adjacent to lung wall in the next slices. This is because the juxta-pleural nodule presents largely beyond our predicted curve range. To resolve the issue, the predicted curve samples $p\left(C_F^n|D^{n-1}\right)$ and the resultant updated contour sample C_F^{*n} should be considered since C_F^{*n} and $p\left(C_F^n|D^{n-1}\right)$ are with relatively low cross-correlation. Thus, further research on the relationship and its solution should be investigated.

To analyze pulmonary disease, the CAD is currently used for the second reader to assist radiologists. In the lung segmentation results from our proposed method, the sensitivity was 95.85% with juxta-plerual nodule detection rate of 96%. In other words, our proposed method results in approximately 5 % false negatives for lung segmentation and 4% missing rate for juxta-pleural nodules. Thus, to be completely used without aid of radiologists, more issues have to be addressed and resolved.

D. VALIDATION FROM OTHER DATABASES
We validated our proposed method from other databases: the Lung Image Database Consortium (LIDC) and chest low dose CT image database (CLD) from Wonkwang University Hospital (WKUH). For the LIDC database, we selected 5 subject image data of 294, 324, 407, 543 and 973, which included juxta-pleural nodules. They included 800 images in total. Among the images, 45 included juxta-pleural nodules. For the CLD, we collected chest CT DICOM images of 5 anonymous

subjects, all of who had juxta-pleural nodules. They included 966 images in total. Among the images, 80 included juxta-pleural nodules. Table 5 summarized the used data.

TABLE 5. Image data summary from LIDC database (5 subjects and 800 image) and chest low dose CT images (5 subjects, 966 images).

	The number of subjects	The number of total images	The number of images including juxta-pleural nodules	Slice thickness	Tube current	Tube voltage
LIDC	5	800	45	1.5~2mm	75~422 mA	120kV
CLD	5	966	80	1mm	84~150 mA	120kV
Total	10	1766	125	1~2 mm	75~422 mA	120kV

To evaluate the performance of the methods, "gold standard" lung contours ($N = 1, 766$) were obtained from two trained radiologists. Initially, one trained radiologist drew the contours, and another trained radiologist confirmed them. We used the same parameters previously simulated in the 16,873 images. We compared the results on the CT images including juxta-pleural nodules from LIDC ($N = 45$) and CLD ($N = 80$). Table 6 and 7 summarize the results from LIDC and CLD databases, respectively. The resultant metrics from LIDC were similar to the results in Table 1. our proposed algorithm outperformed the other three existing methods for both LIDC and CLD. In addition, the juxta-pleural detection rates were 100% and 96%, for LIDC and CLD, respectively.

TABLE 6. Comparison of the performance of the four methods on CT images that included juxta-pleural nodule ($N = 45$) from LIDC database. The DSC, MHD, sensitivity, specificity, accuracy, and juxta-pleural nodule detection rate were evaluated and compared.

Method		CV	NMCV	Snake	Proposed method
DSC	*mean*	0.8767	0.8768	0.8350	0.9769
	std	0.0584	0.0577	0.0591	0.0178
MHD	*mean*	1.5138	1.5026	1.6770	0.4562
	std	0.7570	0.7492	0.8459	0.3626
Sensitivity	*mean*	0.7857	0.7852	0.7213	0.9934
	std	0.0942	0.0930	0.0986	0.0131
Specificity	*mean*	0.9988	0.9985	0.9993	0.9105
	std	0.0032	0.0031	0.0044	0.0754
Accuracy	*mean*	0.8449	0.8450	0.8023	0.9695
	std	0.0754	0.0745	0.0742	0.0193
Detection rate (%)		24%	27%	20%	100%

Finally, we performed our proposed method on all chest CT images from LIDC ($N = 800$) and CLD ($N = 966$). Table 8 and 9 summarize the results from LIDC and CLD databases, respectively. The resultant metrics from both LIDC and CLD were also similar to the results in Table 2. In both, our proposed algorithm also outperformed the other three existing method.

E. DISCUSSION ON EXTENSION CAPABILITY
The automatic lung segmentation is particularly challenging because of juxta-pleural nodules. Although many methods have been proposed for the accurate lung segmentation,

TABLE 7. Comparison of the performance of the four methods on CT images that included juxta-pleural nodule (*N* = 80) from CLD database. The DSC, MHD, sensitivity, specificity, accuracy, and juxta-pleural nodule detection rate were evaluated and compared. The mean and standard deviation are summarized.

Method		CV	NMCV	Snake	Proposed method
DSC	mean	0.8941	0.8956	0.8644	0.9579
	std	0.0568	0.0567	0.0603	0.0436
MHD	mean	1.4799	1.4578	1.5765	0.6817
	std	0.9302	0.9293	0.9415	0.4700
Sensitivity	mean	0.8155	0.8134	0.7659	0.9235
	std	0.0897	0.0895	0.0913	0.0767
Specificity	mean	0.9989	0.9988	0.9999	0.9908
	std	0.0021	0.0019	0.0006	0.0473
Accuracy	mean	0.8640	0.8658	0.8310	0.9605
	std	0.0754	0.0753	0.0774	0.0473
Detection rate (%)		25%	25%	22%	96%

TABLE 8. Results of comparison of the four methods on all chest CT images (*N* = 800) from LIDC database. The DSC, MHD, sensitivity, specificity and accuracy were evaluated. The mean and standard deviation are summarized.

Method		CV	NMCV	Snake	Proposed method
DSC	mean	0.9813	0.9819	0.9658	0.9819
	std	0.0871	0.0871	0.0853	0.0870
MHD	mean	0.3120	0.2696	0.7211	0.3026
	std	0.2579	0.2451	0.3952	0.2445
Sensitivity	mean	0.9743	0.9744	0.9431	0.9751
	std	0.0853	0.0852	0.0857	0.0851
Specificity	mean	0.9996	0.9995	0.9994	0.9993
	std	0.0031	0.0026	0.0033	0.0031
Accuracy	mean	0.9975	0.9976	0.9937	0.9977
	std	0.0035	0.0034	0.0047	0.0032

TABLE 9. Results of comparison of the four methods on all chest CT images (*N* = 966) from CLD database. The DSC, MHD, sensitivity, specificity and accuracy were evaluated. The mean and standard deviation are summarized.

Method		CV	NMCV	Snake	Proposed method
DSC	mean	0.9878	0.9901	0.9746	0.9911
	std	0.0235	0.0225	0.0341	0.0206
MHD	mean	0.3066	0.2445	0.6709	0.2184
	std	0.2654	0.2643	0.5009	0.2074
Sensitivity	mean	0.9828	0.9870	0.9524	0.9914
	std	0.0371	0.0364	0.0458	0.0314
Specificity	mean	1.0000	0.9992	0.9998	0.9989
	std	0.0000	0.0075	0.0004	0.0016
Accuracy	mean	0.9974	0.9978	0.9950	0.9983
	std	0.0033	0.0033	0.0097	0.0025

most lung image segmentation algorithms functioned well only with absent or minimal lung pathologic conditions such as juxta-pleural nodule. Currently, no single segmentation method achieves a globally optimal performance for all cases [47]. For instance, region-based segmentation methods serve as an efficient tool for extracting homogeneous regions such as lungs. However, the methods depend on the magnitude of noise and the precision of the neighborhood criteria; and thus, they suffer from false negatives within the lung region and require demand further post-processing. Recently, the use of prior shape information has gained popularity in medical image segmentation. The methods are either atlas-based or model-based approach to find the lung boundary. Atlas-based approach uses prior shape information of the target organ. The approach consists of a template CT image and the corresponding labels of the thoracic regions. For the segmentation, the template image is registered to the target image. Since the approach is used to align the template to the target image, the accuracy with submillimeter is not provided. The model-based approach similarly uses prior shape information. To better accommodate the shape variabilities, the approach fit either appearance or statistical shapes of lungs to the image. Since it considers both global and local variation of the shape and texture, it is considered effective in handling the abnormal lung segmentation problem. However, similar to atlas-based approach, a representative prior model covering diverse demographics is usually difficult to create. In addition, the performance is limited when the model is not initiated close enough to the actual boundary of the lungs.

In this study, we used the CV model for the global contour, and found the final contour with the juxta-pleural nodule identification based on a Bayesian approach, concave points detection and circle/ellipse Hough transform. Since the CV model method is independent of the rest parts, it can be replaced by other methods such as prior shape methods or region-based methods. Comparing to slice by slice image analysis, the additional Bayesian approach can provide more accurate detection results based on the assumption that the cross-sectional area of the nodule gradually increases and decreases in consecutive axial slices of chest CT scans. Thus, more accurate lung contour segmentation results can be provided by applying to our proposed method framework.

IV. CONCLUSIONS

We have proposed a novel lung contour extraction algorithm capable of detecting juxta-pleural nodules. The algorithm is based on the CV model followed by a Bayesian approach to detect juxta-pleural nodule candidates and eliminate false positives through concave points detection and circle/ellipse Hough transform. In the images that included juxta-pleural nodules (*N* = 314), our method exhibited a DSC of 0.9712, MHD of 0.4504, sensitivity of 0.9711, specificity of 0.9637, accuracy of 0.9667, and juxta-pleural nodule detection rate of 96%, which outperformed the CV model, normalized CV model (NM-CV model), and snake algorithm. Furthermore, in all chest CT images (*N* = 16, 873), our method exhibited a DSC of 0.97091, MHD of 0.5006, sensitivity of 0.9585, specificity of 0.9981, and accuracy of 0.9954, which were also superior to the other models. We believe that our proposed method enhances the accuracy of lung segmentation and can assist radiologists in the interpretation of CT images, particularly for lung-related quantitative analysis.

REFERENCES

[1] L. W. Hedlund, R. F. Anderson, P. Goulding, J. W. Beck, E. L. Effmann, and C. E. Putman, "Two methods for isolating the lung area of a CT scan for density information," *Radiology*, vol. 144, no. 2, pp. 353–357, 1982.

[2] R. Uppaluri, T. Mitsa, M. Sonka, E. Hoffman, and G. Mclemman, "Quatification of pulmonary emphysema from lung CT images using texture analysis," *Amer. J. Resp. Crit. Care Med.*, vol. 156, no. 1, pp. 248–254, 1997.

[3] I. Amirav, S. S. Kramer, M. M. Grunstein, and E. A. Hoffman, "Assessment of methacholine-induced airway constriction by ultrafast high-resolution computed tomography," *J. Appl. Physiol.*, vol. 75, no. 5, pp. 2239–2250, 1993.

[4] R. H. Brown, C. J. Herold, E. A. Zerhouni, W. Mitzner, and C. A. Hirshman, "*InVivo* measurements of airway reactivity using high-resolution computed tomography," *Amer. Rev. Respiratory Disease*, vol. 144, no. 1, pp. 208–212, 1991.

[5] E. A. Hoffman, T. Behrenbeck, P. A. Chevalier, and E. H. Wood, "Estimation of regional pleural surface expansile forces in intact dogs," *J. Appl. Physiol.*, vol. 55, no. 3, pp. 935–948, 1983.

[6] A. M. Boriek, S. Liu, and J. R. Rodarte, "Costal diaphragm curvature in the dog," *J. Appl. Physiol.*, vol. 75, no. 2, pp. 527–533, 1993.

[7] H. A. Gietema *et al.*, "Pulmonary nodules detected at lung cancer screening: Interobserver variability of semiautomated volume measurements," *Radiology*, vol. 241, no. 1, pp. 251–257, 2006.

[8] S. G. Armato and W. F. Sensakovic, "Automated lung segmentation for thoracic CT: Impact on computer-aided diagnosis[1]," *Acad. Radiol.*, vol. 11, no. 9, pp. 1011–1021, 2004.

[9] S. Hu, E. A. Hoffman, and J. M. Reinhardt, "Automatic lung segmentation for accurate quantitation of volumetric X-ray CT images," *IEEE Trans. Med. Imag.*, vol. 20, no. 6, pp. 490–498, Jun. 2001.

[10] M. S. Brown *et al.*, "Method for segmenting chest CT image data using an anatomical model: Preliminary results," *IEEE Trans. Med. Imag.*, vol. 16, no. 6, pp. 828–839, Dec. 1997.

[11] G. J. Kemerink, R. J. S. Lamers, B. J. Pellis, H. H. Kruize, and J. van Engelshoven, "On segmentation of lung parenchyma in quantitative computed tomography of the lung," *Med. Phys.*, vol. 25, no. 12, pp. 2432–2439, 1998.

[12] J. K. Leader *et al.*, "Automated lung segmentation in X-ray computed tomography: Development and evaluation of a heuristic threshold-based scheme[1]," *Academic Radiol.*, vol. 10, no. 11, pp. 1224–1236, 2003.

[13] Y. Masutani, K. Masamune, and T. Dohi, "Region-growing based feature extraction algorithm for tree-like objects," *Vis. Biomed. Comput.*, vol. 1131, pp. 159–171, Feb. 1996.

[14] I. Sluimer, M. Prokop, and B. V. Ginneken, "Toward automated segmentation of the pathological lung in CT," *IEEE Trans. Med. Imag.*, vol. 24, no. 8, pp. 1025–1038, Aug. 2005.

[15] T. Kitasaka, K. Mori, J.-I. Hasegawa, and J.-I. Toriwaki, "Lung area extraction from 3D chest X-ray CT images using a shape model generated by a variable Bézier surface," *Syst. Comput. Jpn.*, vol. 34, no. 4, pp. 60–71, 2003.

[16] S. G. Armato, M. B. Altman, and P. J. L. Rivière, "Automated detection of lung nodules in CT scans: Effect of image reconstruction algorithm," *Med. Phys.*, vol. 30, no. 3, pp. 461–472, 2003.

[17] W.-J. Choi and T.-S. Choi, "Automated pulmonary nodule detection based on three-dimensional shape-based feature descriptor," *Comput. Methods Programs Biomed.*, vol. 113, no. 1, pp. 37–54, 2014.

[18] R. Uppaluri, E. A. Hoffman, M. Sonka, P. G. Hartley, G. W. Hunninghake, and G. McLennan, "Computer recognition of regional lung disease patterns," *Amer. J. Respiratory Crit. Care Med.*, vol. 160, no. 2, pp. 648–654, 1999.

[19] A. A. A. Setio, C. Jacobs, J. Gelderblom, and B. van Ginneken, "Automatic detection of large pulmonary solid nodules in thoracic CT images," *Med. Phys.*, vol. 42, no. 10, pp. 5642–5653, 2015.

[20] S. Dai, K. Lu, J. Dong, Y. Zhang, and Y. Chen, "A novel approach of lung segmentation on chest CT images using graph cuts," *Neurocomputing*, vol. 168, pp. 799–807, Nov. 2015.

[21] X. Chen, J. K. Udupa, U. Bagci, Y. Zhuge, and J. Yao, "Medical image segmentation by combining graph cuts and oriented active appearance models," *IEEE Trans. Image Process.*, vol. 21, no. 4, pp. 2035–2046, Apr. 2012.

[22] L. Zhang, E. A. Hoffman, and J. M. Reinhardt, "Lung lobe segmentation by graph search with 3D shape constraints," in *Proc. SPIE Med. Imag. Physiol. Function Multidimensional Images*, San Diego, CA, USA, vol. 4321, May 2001, pp. 204–215.

[23] P. Hua, Q. Song, M. Sonka, E. A. Hoffman, and J. M. Reinhardt, "Segmentation of pathological and diseased lung tissue in CT images using a graph-search algorithm," in *Proc. IEEE Int. Symp. Biomed. Imag., Nano Macro*, Apr. 2011, pp. 2072–2075.

[24] B. Li, G. E. Christensen, E. A. Hoffman, G. McLennan, and J. M. Reinhardt, "Establishing a normative atlas of the human lung," *Acad. Radiol.* New York, NY, USA: Elsevier, vol. 19, no. 11, pp. 1368–1381, 2012.

[25] L. Zhang and J. Reinhardt, "3D pulmonary CT image registration with a standard lung atlas," in *Physiology and Function from Multidimensional Images*, 2000, pp. 67–77.

[26] L. Zhang, E. A. Hoffman, and J. M. Reinhardt, "Atlas-driven lung lobe segmentation in volumetric X-ray CT images," *IEEE Trans. Med. Imag.*, vol. 25, no. 1, pp. 1–16, Jan. 2006.

[27] J. Benzakoun *et al.*, "Computer-aided diagnosis (CAD) of subsolid nodules: Evaluation of a commercial CAD system," *Eur. J. Radiol.*, vol. 85, no. 10, pp. 1728–1734, 2016.

[28] J. Wang and H. Guo, "Automatic approach for lung segmentation with juxta-pleural nodules from thoracic CT based on contour tracing and correction," *Comput. Math. Methods Med.*, vol. 2016, Oct. 2016, Art. no. 2962047.

[29] G. Aresta, A. Cunha, and A. Campilho, "Detection of juxta-pleural lung nodules in computed tomography images," in *Proc. SPIE Med. Imag. Comput.-Aided Diagnosis Med. Imag.*, Orlando, FL, USA, vol. 10134, 2017, p. 101343N.

[30] R. Vishraj, S. Gupta, and S. Singh, "Intuitionistic fuzzy domain level set method for automatic delineation of juxta-pleural pulmonary nodules in thoracic CT images," *Current Med. Imag. Rev.*, vol. 14, no. 2, pp. 280–288, 2018.

[31] T. F. Chan and L. A. Vese, "Active contours without edges," *IEEE Trans. Image Process.*, vol. 10, no. 2, pp. 266–277, Feb. 2001.

[32] G. Cao, Z. Mao, X. Yang, and D. Xia, "Optical aerial image partitioning using level sets based on modified Chan–Vese model," *Pattern Recognit. Lett.*, vol. 29, no. 4, pp. 457–464, 2008.

[33] T. F. Chan, B. Y. Sandberg, and L. A. Vese, "Active contours without edges for vector-valued images," *J. Vis. Commun. Image Represent.*, vol. 11, no. 2, pp. 130–141, 2000.

[34] N. Zhang, J. Zhang, and R. Shi, "An improved chan-vese model for medical image segmentation," in *Proc. Int. Conf. Comput. Sci. Softw. Eng.*, Dec. 2008, pp. 864–867.

[35] P. Annangi, S. Thiruvenkadam, A. Raja, H. Xu, X. Sun, and L. Mao, "A region based active contour method for X-ray lung segmentation using prior shape and low level features," in *Proc. IEEE Int. Symp. Biomed. Imag., Nano Macro*, Apr. 2010, pp. 892–895.

[36] T. F. Chan and L. A. Vese, "Active contours without edges," *IEEE Trans. Image Process.*, vol. 10, no. 2, pp. 266–277, Feb. 2001.

[37] M.-P. Dubuisson and A. K. Jain, "A modified Hausdorff distance for object matching," in *Proc. 12th IAPR Int. Conf. Pattern Recognit. Comput. Vis. Image Process.*, Oct. 1994, pp. 566–568.

[38] S. Gao, J. Yang, and Y. Yan, "A local modified Chan–Vese model for segmenting inhomogeneous multiphase images," *Int. J. Imag. Syst. Technol.*, vol. 22, no. 2, pp. 103–113, 2012.

[39] S. Guo and L. Wang, "Automatic CT image segmentation of the lungs with an iterative Chan-Vese algorithm," in *Proc. Int. Conf. Informat., Electron. Vis. (ICIEV)*, 2015, pp. 1–4.

[40] C. W. Bong, C. C. Liew, and H. Y. Lam, "Ground-glass opacity nodules detection and segmentation using the snake model," *Bio-Inspired Computation and Applications in Image Processing*. Amsterdam, The Netherlands: Elsevier, 2017, pp. 87–104.

[41] P. Getreuer, "Chan-vese segmentation," *Image Process. Line*, vol. 2, pp. 214–224, Aug. 2012.

[42] X. Jiang, R. Zhang, and S. Nie, "Image segmentation based on level set method," *Phys. Procedia*, vol. 33, pp. 840–845, 2012.

[43] H. MacMahon *et al.*, "Guidelines for management of incidental pulmonary nodules detected on CT images: From the Fleischner Society 2017," *Radiology*, vol. 284, no. 1, pp. 228–243, 2017.

[44] T. J. Atherton and D. J. Kerbyson, "Size invariant circle detection," *Image Vis. Comput.*, vol. 17, no. 11, pp. 795–803, Sep. 1999.

[45] J. P. Chopin, S. J. Miklavcic, and H. Laga, "Selection of parameters in active contours for the phenotypic analysis of plants," in *Proc. 20th Int. Congr. Modelling Simulation*, 2013, pp. 510–516.

[46] F. Precioso, M. Barlaud, T. Blu, and M. Unser, "Robust real-time segmentation of images and videos using a smooth-spline snake-based algorithm," *IEEE Trans. Image Process.*, vol. 14, no. 7, pp. 910–924, Jul. 2005.

[47] A. Mansoor *et al.*, "Segmentation and image analysis of abnormal lungs at CT: Current approaches, challenges, and future trends," *RadioGraphics*, vol. 35, no. 4, pp. 1056–1076, 2015.